Interference in spin-orbit coupled transverse magnetic focusing: Emergent phase due to in-plane magnetic fields

Samuel Bladwell and Oleg P. Sushkov
School of Physics, University of New South Wales, Sydney 2052, Australia

(Received 28 February 2018; published 30 August 2018)

Spin-orbit (SO) interactions in two dimensional systems split the Fermi surface and allow for the spatial separation of spin states via transverse magnetic focusing (TMF). In this paper, we consider the case of combined Rashba and Zeeman interactions, which leads to a Fermi surface without cylindrical symmetry. While the classical trajectories are effectively unchanged, we predict an additional contribution to the phase, linear in the applied in-plane magnetic field. We show that this term is unique to TMF and vanishes for magnetic (Shubnikov de Haas) oscillations. Finally we propose some experimental signatures of this phase.

DOI: 10.1103/PhysRevB.98.085438

I. INTRODUCTION

Transverse magnetic focusing (TMF) has a long history, being employed in metals and semiconductors, and has been used to investigate the shape of the Fermi surface [1–5]. A TMF experiment consists of a source and a detector, separated by a distance l, with charges focused from the source to the detector via a weak transverse magnetic field. It is the direct translation of charge mass spectroscopy to the solid state. Despite the nearly half century of experimental history, TMF is still producing novel results, with the most recent application in systems with nonquadratic dispersion relations, such as graphene [6] and two-dimensional charge gases with large spin-orbit (SO) interactions [7]. In SO coupled systems, the spin-split Fermi surfaces result in a "doubled" focusing peak, which provides platform investigations of polarization effects in the source and detector quantum point contacts [8,9]. The separation of the peaks also allows for the direct determination of the magnitude of the spin-orbit splitting, hence TMF can be used in addition to quantum magnetic oscillations to yield detailed information about SO coupled electron and hole systems.

Much of the theoretical and experimental work concerning TMF with large spin-orbit splittings has considered a singular dominant SO interaction. This leads to a cylindrically symmetric Fermi surface and a double peak structure that is, in essence, two copies of the single peak structure [10]. This assumption is well justified for many typical experimental systems grown along high symmetry crystal axes, as classical trajectories are not significantly altered except in the case of extremely large asymmetry [11]. While a sufficiently large secondary SO interaction can lead to magnetic breakdownlike behavior [12], the requirement for resolution of the double peak structure means that the typical regime is characterized by the secondary SO interaction being weaker than the primary interaction that yields the double peak structure of spin-split TMF.

Like earlier studies in semiconductors, SO coupled systems have Fermi wavelengths comparable to the feature size making interference an important feature of the magnetic focusing spectrum [5,13]. With the addition of SO coupling, the interference effects are further enriched and yield new methods of studying SO interactions. In this paper, we focus on the problem of interference in TMF in systems with a Rashba SO interaction and an applied in plane magnetic field. This combination of interactions results in a spin-split Fermi surface without cylindrical symmetry. Due to the large prefactors, proportional to the Fermi momentum and focusing length, relatively small in plane fields can lead to large phase contributions. While the classical trajectories are effectively unchanged, an additional phase term emerges, linear in the applied magnetic field. We show that this additional contribution to the phase can significantly alter the TMF interference spectrum.

Our paper is organized as follows. In Sec. II we present the classical trajectories for magnetic focusing and introduce the relevant Hamiltonian. Following on from this, in Sec. III we develop a theory of interference in the absence of cylindrical symmetry, building on previous work on interference in TMF with SO coupling [13]. Finally, in Sec. IV we consider some relevant examples, with a minimalistic model of the injector and detector wave functions.

II. SPIN-ORBIT INTERACTIONS AND CLASSICAL TRAJECTORIES

Semiconductor heterostructures allow for a great diversity of SO interactions. While the approach we will detail is general, for specificity we will consider two interactions; the Rashba interaction resulting from a lack of surface inversion symmetry in the sample, and the Zeeman interaction due to an applied in plane magnetic field. These two interactions have the advantage of being tunable. In electron systems, the Rashba interaction has the kinematic structure [14],

$$\mathcal{H}_{R,e} = i\frac{\gamma_1}{2}p_-\sigma_+ + \text{H.c.}$$
$$\sigma_\pm = \sigma_x \pm i\sigma_y \quad p_\pm = p_x + ip_y, \tag{1}$$

where γ_1 is material parameter dependent on the electric field perpendicular to the two-dimensional plane. The Pauli matrices σ correspond to electron spin $s = 1/2$, and the selection rule for $\sigma_\pm$ is $\Delta s_z = \pm 1$. Spin splitting in the magnetic focusing spectrum was recently observed in InGaAs quantum wells [15]. In GaAs heterostructures, the spin-orbit interaction is typically not large enough to obtain a spin-split magnetic focusing spectrum. Heavy hole gases can also be engineered to have a Rashba spin orbit interaction [16]. Due to the heavy holes having angular momentum $J_z = \pm 3/2$, the Rashba interaction arises from the combined action of both the Luttinger, $(\mathbf{p}\cdot\mathbf{J})^2$, and Rashba terms, $\mathbf{p}\cdot(\mathbf{J}\times\mathbf{z})$, with $\mathcal{H}_R \propto (\boldsymbol{J}\cdot\boldsymbol{p})^2(\boldsymbol{p}\cdot\mathbf{J}\times\mathbf{z})$. Typically, the light holes $J_z = \pm 1/2$, have significantly higher energy, and it is more convenient to work in the subspace spanned by the Pauli matrices, with $J_\pm^3 \to \sigma_\pm$. The selection rule is $\Delta J_z = \pm 3$. In this subspace the kinematic structure is [16]

$$\mathcal{H}_{R,h} = i\frac{\gamma_3}{2}p_-^3\sigma_+ + \text{H.c.}, \tag{2}$$

where γ_3 is a material parameter analogous to γ_1.

To induce an asymmetry in the spin-split Fermi surface, we consider an applied in plane magnetic field. For electrons, this results in the usual Zeeman interaction,

$$\mathcal{H}_{Z,e} = \frac{g}{2}\mu_B B_-\sigma_+ + \text{H.c.}, \tag{3}$$

where g is the electron g factor, and $B_\pm = B_x \pm iB_y$. There is no equivalent expression for heavy holes, as $J_z = \pm 3/2$ cannot be coupled directly, but requires the combined action of Zeeman, $\mathbf{J}\cdot\mathbf{B}$, and Luttinger, $(\mathbf{p}\cdot\mathbf{J})^2$, with $\mathcal{H}_{Z,h} \propto (\boldsymbol{J}\cdot\boldsymbol{p})^2(\boldsymbol{J}\cdot\boldsymbol{B})$. The kinematic structure is

$$\mathcal{H}_{Z,h} = \frac{g_1}{2}\mu_B p_-^2 B_-\sigma_+ + \text{H.c.}, \tag{4}$$

where we use the aforementioned subspace of heavy holes [17,18].

We use a dimensionless form of the coefficients γ_3 in Eq. (2) and γ_1 in Eq. (1),

$$\begin{aligned}\gamma_1 &= \tilde{\gamma}_1\frac{\epsilon_F}{k_F}\\ \gamma_3 &= \tilde{\gamma}_3\frac{\epsilon_F}{k_F^3}\\ k_F &= \sqrt{2m\epsilon_F},\end{aligned} \tag{5}$$

where ϵ_F is the Fermi energy (chemical potential). The dimensionless coefficient $\tilde{\gamma}_{1,3}$ represents the value of the SO interaction at $p = k_F$ in units of the Fermi energy. This can be directly related to the splitting of the "double" TMF peaks. For the heavy holes Rashba interaction, $\tilde{\gamma}_3$ can be as large as $|\tilde{\gamma}_3| \sim 0.1$–$0.2$, in GaAs depending on the z confinement [16]. For the electron Rashba interaction, in InGaAs quantum wells, $\tilde{\gamma}_1 \sim 0.2$ [15]. For the Zeeman interaction in holes, we consider the dimensionless coefficient, $\tilde{g}_1$,

$$\tilde{g}_1 = g_1 k_F^2. \tag{6}$$

For GaAs heavy hole quantum wells, $\tilde{g}_1 \sim 1$ [17,18]. The electron g factor in InGaAs quantum wells is $g \sim -9$ [19].

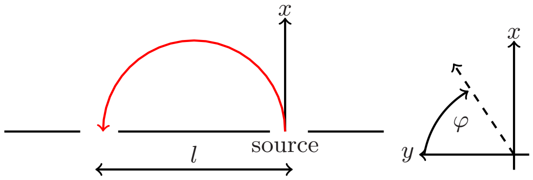

FIG. 1. The focusing setup with focusing length l. We choose axis x and y such that x is aligned along the axis of injection. We locate the source at $(x, y) = (0, 0)$. The in plane magnetic field angle φ is measured from the y axis. The dashed line indicates the magnetic field orientation.

We can consider the SO interaction as a momentum dependent effective Zeeman magnetic field, $\mathcal{B}(\mathbf{p})$. Hence the Hamiltonian is

$$\begin{aligned}\mathcal{H} &= \frac{\mathbf{p}^2}{2m} + \mathcal{B}(\mathbf{p})\cdot\boldsymbol{\sigma}\\ \boldsymbol{\sigma}\cdot\mathcal{B}(\mathbf{p}) &= \mathcal{H}_R + \mathcal{H}_Z\end{aligned} \tag{7}$$

with the application of a transverse magnetic field, B_z, $\mathbf{p} \to \boldsymbol{\pi} = \mathbf{p} - e\mathbf{A}$, with the vector potential chosen in an appropriate gauge, $\mathbf{A} = B_z(0, -x, 0)$. The semiclassical dynamics of the charge carriers are characterized by cyclotron orbits [11], with a cyclotron radius, $r_c = k_F/eB_z$, and a cyclotron frequency, $\omega_c = eB_z/m$. Due to the curvature of the trajectories, the effective magnetic field $\mathcal{B}$ evolves in time. Since TMF experiments are typically performed at relatively small transverse magnetic fields, $B_z \leqslant 0.1$ T, the spin adiabatically follows the effective magnetic field, $\mathcal{B}$. Provided $|\mathcal{B}| \gg \omega_c$, the spin states evolve adiabatically, and consequently there is no tunneling between the spin states. We note that this is also a condition for a "double" focusing peak.

We are now in a position to explore the semiclassical dynamics. The Hamiltonian, with an applied magnetic field $\mathbf{B}$, is (Fig. 1)

$$\begin{aligned}\mathcal{H} &= \frac{\boldsymbol{\pi}^2}{2m} + \boldsymbol{\sigma}\cdot\mathcal{B}\\ \mathbf{B} &= (B_{||}\cos\varphi, B_{||}\sin\varphi, B_z)\\ \boldsymbol{\pi} &= \mathbf{p} - e\mathbf{A},\end{aligned} \tag{8}$$

where φ is the field angle, $B_{||}$ is the in plane magnetic field, and B_z is the (weak) transverse focusing field. We stress that typically $B_z \sim 0.1$ T, while $B_{||}$ can be a few Teslas for heavy hole quantum well in GaAs [7]. For electrons in InGaAs, $B_{||} \sim 1$ T due to the much larger g factor in these systems. If the spin follows the effective field adiabatically, $\boldsymbol{\sigma} \to s\mathcal{B}/|\mathcal{B}|$, where s is a pseudoscalar and describes the two possible spin states. The resulting adiabatic Hamiltonian is

$$\begin{aligned}\mathcal{H}_{\text{cl}} &= \frac{\boldsymbol{\pi}^2}{2m} + s|\mathcal{B}|\\ \boldsymbol{\pi} &= |\boldsymbol{\pi}|(\cos\phi, \sin\phi, 0),\end{aligned} \tag{9}$$

where ϕ is the azimuthal angle (see Fig. 2). The semiclassical dynamics of this Hamiltonian has been found with expansion in powers of $|\mathcal{B}|/\varepsilon_F$ [11]. This is valid in the regime $\omega_c \ll$

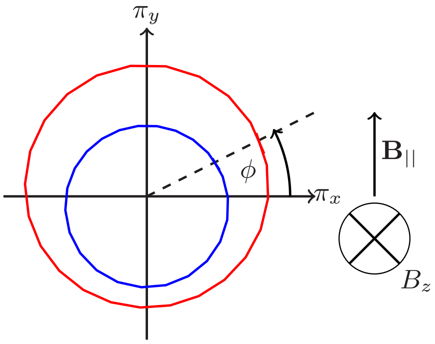

FIG. 2. A cartoon of the trajectories in momentum space with a Rashba spin orbit interaction, with an applied in plane magnetic field, $\mathbf{B}_{||}$. Red (blue) surface has $s = -1$ ($s = 1$). The azimuthal angle ϕ of the momentum, π, is presented, with π_x and π_y given by Eq. (9).

$|\mathcal{B}| \ll \epsilon_F$. The effective magnetic field, $\mathcal{B}$, is

$$\begin{aligned} &|\mathcal{B}| = \epsilon_F|\tilde{\gamma}_3|b(\phi)\\ &b(\phi) =\rightarrow\\ &= \sqrt{1 + 2(\tilde{g}_1\mu_B/\tilde{\gamma}_3\varepsilon_F)B_{||}\cos(\phi-\varphi) + (\tilde{g}_1\mu_B/\tilde{\gamma}_3\varepsilon_F)^2B_{||}^2} \end{aligned} \tag{10}$$

for holes and

$$\begin{aligned} &|\mathcal{B}| = \epsilon_F|\tilde{\gamma}_1|b(\phi)\\ &b(\phi) =\rightarrow\\ &= \sqrt{1 + 2(g\mu_B/\tilde{\gamma}_1\varepsilon_F)B_{||}\cos(\phi-\varphi) + (g\mu_B/\tilde{\gamma}_1\varepsilon_F)^2B_{||}^2} \end{aligned} \tag{11}$$

for electrons. Evidently, these effective magnetic fields are identical, and the dynamics of electrons and holes are the same in this adiabatic semiclassical approach, despite the kinematic structure of the spin-orbit interactions, Eqs. (2) and (1) being markedly different. For clarity, in the following calculations, we will exclusively refer to holes.

The equations of motion of this classical Hamiltonian are

$$\begin{aligned} v_+ &= \frac{\partial\mathcal{H}_{\rm cl}}{\partial\pi_-} = \frac{\pi_+}{m} - \frac{s}{|\mathcal{B}|}\frac{\partial\mathcal{B}^2}{\partial\pi_-}\\ \dot{\pi}_+ &= i\omega_c m v_+. \end{aligned} \tag{12}$$

The solution to these classical equations of motion has been found with expansion in powers of $|\mathcal{B}|/\varepsilon_F$ [11]. The particle trajectories are given by

$$\begin{aligned} \phi_0 &= \omega_c t\\ \phi &= \phi_0 - s\frac{3|\tilde{\gamma}_3|}{2}\int_{\phi_i}^{\phi_0}\frac{a(\phi')}{b(\phi')}d\phi'\\ x + iy &= \frac{k_F}{m\omega_c}\Big\{i(e^{i\phi_i} - e^{i\phi})\\ &\quad + s\frac{|\tilde{\gamma}_3|}{2}\int_{\phi_i}^{\phi} e^{i\phi'}\Big[b(\phi') + 3i\frac{c(\phi')}{b(\phi')}\Big]d\phi'\Big\}, \end{aligned} \tag{13}$$

where $k_F = \sqrt{2m\epsilon_F}$ is the Fermi momentum, and ϕ is the azimuthal angle. We have introduced the initial azimuthal angle ϕ_i. The condition of the spin adiabaticity implies that $b(\phi)$ does not vanish, $|\tilde{\gamma}_3|b(\phi) \gg \omega_c/\epsilon_F$. The functions $c(\phi)$ and $a(\phi)$ are given by

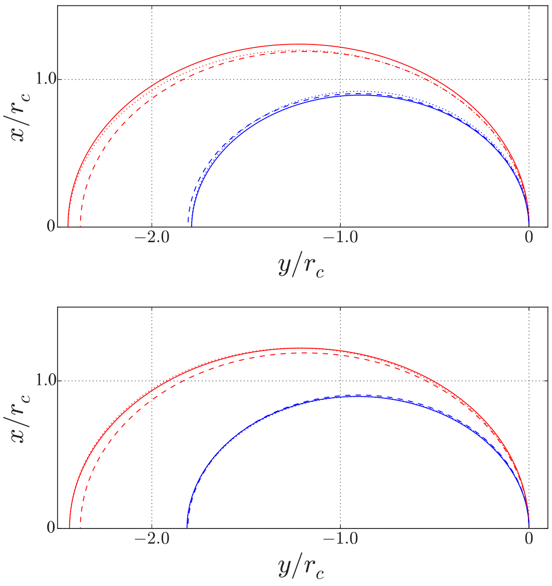

FIG. 3. Trajectories of spin-orbit coupled holes, with $s = 1$ in red, and $s = -1$ in blue. We use $\tilde{\gamma}_3 = 0.25$ and $\tilde{g}_1 = 1$ with an in plane magnetic field, $B_{||} = 4$ T. The Fermi energy is $\varepsilon_F = 1.9$ meV. The upper panel has a in plane magnetic field orientation $\varphi = 0$, while the lower panel has a field orientation $\varphi = \pi/2$. We present the trajectories normalized with the cyclotron radii, with $r_c \approx l/2$. The dashed lines in the upper and lower panel have $B_{||} = 0$ T. Note that the change in the trajectory is very small. We note that the injection with velocity directed fully along x does not correspond to $\phi_i = 0$.

$$\begin{aligned} \dot{\phi} &= \omega_c\left[1 - s\frac{3|\tilde{\gamma}_3|}{2}\frac{a(\phi)}{b(\phi)}\right]\\ a(\phi) &= 1 + (5/3)(\tilde{g}_1\mu_B|B_{||}|/\tilde{\gamma}_3\varepsilon_F)\cos(\phi-\varphi)\\ &\quad + (2/3)(\tilde{g}_1\mu_B|B_{||}|/\tilde{\gamma}_3\varepsilon_F)^2\\ c(\phi) &= \frac{1}{3}(\tilde{g}_1\mu_B|B_{||}|/\tilde{\gamma}_3\varepsilon_F)\sin(\phi-\varphi)\,. \end{aligned} \tag{14}$$

These solve the problem of the classical motion. We have presented illustrative trajectories in Fig. 3. The classical trajectories are essentially unchanged, even up to several Tesla.

A peculiar feature to note is that $\phi_i = 0$ does not correspond to the classical trajectory, since $\phi_i = 0$ has nonzero v_y. We define the physical injection angle θ such that the classical trajectories shown in Fig. 3 correspond to injection with $\theta = 0$, with θ measured from the x axis. To relate this to ϕ_i, we differentiate Eq. (13) to obtain v_y at the source

$$\begin{aligned} v_y &\approx \frac{k_{F,s}}{m}\left(\sin\phi_i + \frac{\tilde{g}_1\mu_B B_{||}}{2}\sin(2\phi_i + \varphi)\right)\\ k_{F,s} &= k_F\left(1 + s\frac{\tilde{\gamma}_3}{2\varepsilon_F}\right). \end{aligned} \tag{15}$$

Setting $v_y = 0$ and solving, we obtain $\phi_i \approx \tilde{g}_1\mu_B B_{||}\sin\varphi/2\varepsilon_F$. In general, θ is related to ϕ_i by

$$\phi_i = \theta + \frac{\tilde{g}_1\mu_B B_{||}\sin\varphi}{2\varepsilon_F}. \tag{16}$$

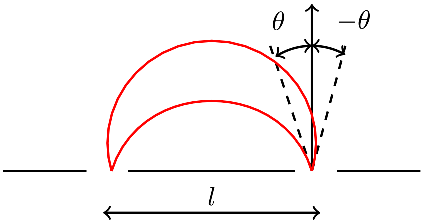

FIG. 4. The two trajectories of injection angle θ and $-\theta$, measured from the x axis at the point of injection.

We stress again that the method used here, and following in Sec. III, can equally be applied to electron systems with a Rashba SO interaction and an applied in-plane magnetic field. Finally, we note that the semiclassical method employed to determine the trajectories can be easily adapted to include additional SO interactions [11]. In the case of Dresselhaus SO interactions arising from crystal anisotropy [16], this will include an additional angle relating to the lattice orientation relative to the device.

III. INTERFERENCE

The problem of interference in systems with large SOIs has been treated in detail for cylindrically symmetric systems [13]. Like any interference problem, there are two trajectories (see Fig. 4) connecting the source located at the origin, (0, 0), to a detector located at $(0, l)$. These two paths are defined by injection angles $\pm\theta$, with (Fig. 4)

$$\cos\theta = \frac{l}{2r_{c,s}}$$
$$r_{c,s} = k_{F,s}/eB_z. \tag{17}$$

Interference arises from the difference between the phases of the two trajectories, with the semiclassical propagator defined as the sum over the two classically allowed paths,

$$K(\theta) \sim e^{i\mathcal{S}(\theta)} + e^{i\mathcal{S}(-\theta)} \tag{18}$$

with the phase $\mathcal{S} \propto \int \boldsymbol{p}\cdot d\boldsymbol{l}$, where $d\boldsymbol{l}$ is integrated along the path of the trajectories. In a typical TMF setup, the source and detector are of some finite aperture, with the Huygens kernel Eq. (18) averaged over this aperture [13].

Evaluation of the phase is treated analogously to the cylindrically symmetric case. The canonical is related to the kinematic momentum and the vector potential by $\boldsymbol{p} = m\boldsymbol{v} + e\boldsymbol{A}$, and the action is

$$\mathcal{S}(\theta) = \int_{\delta S} (m\boldsymbol{v} + e\boldsymbol{A})\cdot d\boldsymbol{l}, \tag{19}$$

where $\boldsymbol{v}$, $\boldsymbol{A}$, $d\boldsymbol{l}$, and the path, δS, are dependent on $\tilde{g}_1\mu_B B_{||}$. Using the previously determined equations of motion, Eqs. (13) and (14), the phase integral, Eq. (19), can be converted into an integral over the azimuthal angle, ϕ',

$$\mathcal{S}(\theta) = eB_z \int_{\phi_i}^{\phi} \left(\left(\frac{dx}{d\phi'}\right)^2 + \left(\frac{dy}{d\phi'}\right)^2 - x\frac{dy}{d\phi'} \right) d\phi'. \tag{20}$$

The relationship between the physical injection angle θ and ϕ_i is presented in Eq. (16). We must also determine ϕ in terms of θ.

The trajectory from the source to the detector is, in terms of the azimuthal angle, from ϕ_i to ϕ. This corresponds to the spatial positions (0, 0) and $(0, l)$, respectively. From Eq. (13) we have

$$x = 0 = \frac{k_s}{\omega_c m}\left\{(\sin\phi_i + \sin\phi) + s\frac{\tilde{g}_1\mu_B B_{||}}{4}[\sin(2\phi - \varphi) - \sin(2\phi_i - \varphi)]\right\}. \tag{21}$$

We have restricted ourselves to a first order expansion in $\tilde{g}_1\mu_B B_{||}$ when performing the integration of Eq. (13). The trajectory deviates only minimally from the arc of a circle (see Fig. 3), and we can reasonably employ the approximation $\phi \approx \pi - \phi_i$ for the $\tilde{g}_1\mu_B B_{||}$ dependent terms. With this approximation, solving Eq. (22) we obtain

$$\phi \approx \pi - \phi_i - s\tilde{g}_1\mu_B B_{||}\sin\phi_i\cos\varphi. \tag{22}$$

Finally, this can be expressed in terms of the injection angle, θ using Eq. (16), to obtain the integration limits for Eq. (20) in terms of θ.

Using these integration limits, integration of Eq. (20) yields

$$S(\theta) = \frac{k_s^2}{2eB}\{\pi - 2\theta + \sin 2\theta + \zeta - s\tilde{g}_1\mu_B B_{||}\sin\theta(1 - \cos 2\theta)\cos\varphi\}$$
$$\zeta = \tilde{g}_1\mu_B B_{||}\left\{\sin\varphi - \cos 2\theta\sin\varphi + \sin\varphi\left(\cos\theta + \frac{1}{3}\cos^3\theta\right)\cos\varphi\left(\cos\theta + \frac{1}{3}\cos^3\theta\right)\right\}. \tag{23}$$

For $-\theta$ injection angles, we take $\theta \to -\theta$. We have introduced here ζ which contains the phase terms that do not contribute any net phase difference, that are symmetric for $\theta \to -\theta$. According to Eq. (18), we then have

$$K(\theta) \sim e^{i\mathcal{S}(\theta)} + e^{i\mathcal{S}(-\theta)}$$
$$\sim \sin\left[\frac{k_s^2}{2eB}(2\theta - \sin 2\theta + s\tilde{g}_1\mu_B B_{||}\sin\theta(1 - \cos 2\theta)\cos\varphi) + \frac{\pi}{4}\right]. \tag{24}$$

The additional factor of $\pi/4$ arises due to the caustic for the $-\theta$ path [13]. The third line of Eq. (24), which is linear in $\tilde{g}_1\mu_B B_{||}$, represents the "emergent phase contribution," and is the first major result of this work. This term is particularly remarkable, since the classical trajectories have no first order dependence on $\tilde{g}_1\mu_B B_{||}$. For quantum (Shubnikov de Haas) oscillations, the integral is over the entire Fermi surface, and this term vanishes. Thus it is peculiar to the particular geometry of TMF, which defines the angle φ between the in plane magnetic field and the injector.

It is instructive to examine the variation in the interference fringe separation due to the application of the in magnetic plane

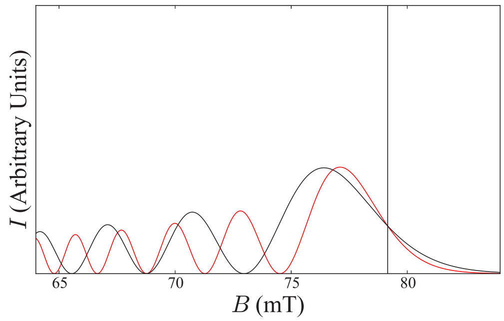

FIG. 5. Interference pattern calculated for pointlike source and detector from Eq. (28). We use $l = 1500$ nm, $k_F = 0.107 \times 10^{-1}$ nm^{-1} with a Rashba splitting $\tilde{\gamma}_3 = 0.3\varepsilon_F$, and $\tilde{g}_1\mu_B B_{||} = 0.15\varepsilon_F$, corresponding to $B_{||} \sim 4$–5 T for $\tilde{g}_1 = 1$ and $\varepsilon_F \approx 2$ meV. For clarity we present only a single spin state. The interference spectrum is calculated from Eq. (28), with a black vertical line indicating the location of the classical cutoff. Red plots in-plane field with $\varphi = \pi$; black has $\varphi = 0$.

field, expanding for small θ. For small θ, according to Eq. (18),

$$\theta \approx \sqrt{\frac{2r_{c,s} - l}{r_{c,s}}} = \sqrt{\frac{y}{r_{c,s}}}; \tag{25}$$

here $y = 2r_{c,s} - l$ is the detuning from the focusing length, l, which marks the boundary of the classically forbidden region. For small θ, Eq. (24) becomes

$$K(y) \approx \sin\left(\frac{2}{3}\nu_s\left(\frac{y}{r_c}\right)^{\frac{3}{2}}\left(1 + s\frac{3}{2}\tilde{g}_1\mu_B B_{||}\cos\varphi\right) + \frac{\pi}{4}\right) \tag{26}$$

and from Eq. (26), we find a characteristic spacing of the interference fringes to be

$$\frac{\delta B}{B} \approx \frac{2.2}{2\nu^{\frac{2}{3}}}(1 - s\tilde{g}_1\mu_B B_{||}\cos\varphi), \tag{27}$$

where δB is the fringe spacing. This provides a method of determining the strength of the in plane g factor. For other alternative SO interaction combinations, for instance, Dresselhaus and Rashba SO interactions, we anticipate a similar dependence. As can be seen in Fig. 5, even for the first interference fringe, there is a measurable shift. While there is no direct enhancement, $\tilde{g}_1\mu_B B_{||} \sim 0.1\varepsilon_F$ at fields of a few Tesla in hole systems. Recent TMF experiments have resolved a single interference fringe for the low field peak [7,15], which would be sufficient for the determination of $\tilde{g}_1\mu_B B_{||}$.

The remaining elements of the Huygen's kernel are unchanged in the cyclindrically symmetric case. As was detailed in Ref. [13], the asymptotic form of the Huygen's kernel can be related to the Airy function. Employing the same reasoning, from Eqs. (24) and (26), we obtain

$$K_s = e^{i\frac{\pi(\nu_s - 1 - n)}{2}}\frac{\nu_s^{2/3}}{2\sqrt{2}r_{\mathrm{cs}}}\left[(\sigma_z - is\sigma_x)Ai(\overline{y}_s) + \frac{n}{\nu_s^{1/3}}Ai'(\overline{y}_s)\right]. \tag{28}$$

Here $\overline{y} = y\nu_s^{2/3}(1 + s\tilde{g}_1\mu_B B_{||}\cos\varphi)/r_c$. We present plots of the resulting interference spectrum in Fig. 5 with pointlike sources and detectors, for both the classical form of the Huygen's kernel and Eq. (28). We stress that this semiclassical approach employed is only valid if $\nu_s \gg 1$. For typical experimental systems, $\nu_s > 30$.

IV. DISCUSSION

In real systems, the source and detector have finite size and can influence the observed interference pattern. Typically experimental devices use quantum point contacts, which consist of a narrow channel connecting a reservoir to the 2DHG. These have some characteristic width, w, and can be modeled by standing waves in the y direction,

$$\psi_s \propto \chi_s \sin\left(\frac{\pi y}{w}\right) \quad 0 < y < w$$
$$\psi_d \propto \chi_d \sin\left(\frac{\pi(y - L)}{w}\right) \quad L < y < L + w, \tag{29}$$

where w is the width of the channel, and χ_s and χ_d are the eigenspinors at the source and detector, respectively [13]. The exit width, w, is imposed by the lithographic geometry of the QPC [20], however can vary depending on the conductance. We consider a hole gas with a density, $n = 1.85\ 10^{11}$ cm^{-2}, and corresponding Fermi momentum, $k_F = 0.107$ nm^{-1}. With a Rashba splitting of $\tilde{\gamma}_3 = 0.2\varepsilon_F$, the smaller spin-split Fermi momentum will be $k_- = 0.096$ nm^{-1} ($\lambda \approx 66$ nm) and the larger Fermi momentum $k_+ = 0.118$ nm^{-1} ($\lambda \approx 53$ nm). The distance between the source and the detector is $L = 1500$ nm. The corresponding magnetic field at the classical edge of the bright region for k_- is $B_- = 77mT$, while for k_+, $B_+ = 94mT$. We will start by considering a QPC of width $w = 150$ nm, which we note corresponds to the lithographic width of the device of Ref. [7]. The resulting focusing spectrum is presented in Fig. 6. While interference fringes are still visible, they are suppressed, and the additional phase contribution manifests as a suppression or enhancement of the spin-split focusing peaks. We note that this experimental signature is similar to that typically attributed to polarization in the QPCs [12].

In summary, we have employed Huygen's principle to determine quantum interference for systems with asymmetrical

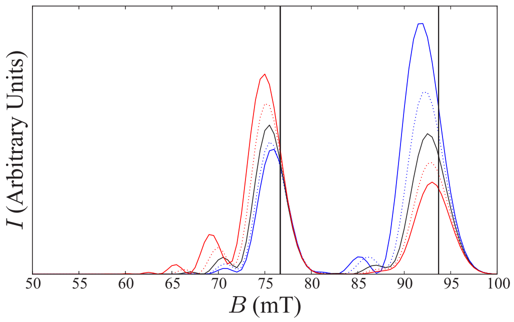

FIG. 6. Interference patterns versus $\tilde{g}_1\mu_B B_{||}$, with range $-0.1 < \tilde{g}_1\mu_B B_{||} < 0.1$, with $\varphi = 0$. Here $l = 2000$ nm, $w = 150$ nm. Positive $\tilde{g}_1\mu_B B_x$ is presented in red, while negative $\tilde{g}_1\mu_B B_x$ are in blue. The $B_x = 0$ TMF spectrum is a solid black curve. Vertical black lines indicate the location of the classical maximum, $B_{\mathrm{focusing}} = 2\hbar k_s/el$.

Fermi surfaces. While in this work we focus on a specific case of an in-plane magnetic field in combination with a Rashba spin-orbit interaction, the method employed is general. We have predicted an emergent phase contribution, linear in the applied in plane magnetic field, despite there being no first order changes to the classical trajectories. This emergent phase term significantly alters the interference spectrum of TMF. We propose that this could be used to measure the in plane g factor.

ACKNOWLEDGMENTS

We thank Alex Hamilton, Dmitry Misarev, Harley Scammell, and Matthew Rendell for their helpful discussions. S.S.R.B. acknowledges the support of the Australian Postgraduate Award. This research was partially supported by the Australian Research Council Centre of Excellence in Future Low-Energy Electronics Technologies (Project No. CE170100039) and funded by the Australian Government.

[1] Yu. V. Sharvin, Zh. Eksp. Teor. Fiz. **48**, 984 (1965) [Sov. Phys. JETP **21**, 655 (1965)].

[2] Yu. V. Sharvin and L. M. Fisher, Pis'ma Zh. Exp. Teor. Fiz. **1**, 54 (1969) [Sov. Phys. JETP Lett. **1**, 152 (1965)].

[3] V. S. Tsoi, Pis'ma. Zh. Exp. Teor. Fiz. **19**, 114 (1974) [Sov. Phys. JETP Lett. **19**, 70 (1974)].

[4] V. S. Tsoi, J. Bass, and P. Wyder, Rev. Mod. Phys. **71**, 1641 (1999).

[5] H. van Houten, C. W. J. Beenakker, J. G. Williamson, M. E. I. Broekaart, P. H. M. van Loosdrecht, B. J. van Wees, J. E. Mooij, C. T. Foxon, and J. J. Harris, Phys. Rev. B **39**, 8556 (1989).

[6] T. Taychatanapat, K. Watanabe, T. Taniguchi, and P. Jarillo-Herrero, Nat. Phys. **9**, 225 (2013).

[7] L. P. Rokhinson, V Larkina, Y. B. Lyanda-Geller, L. N. Pfeiffer, and K. W. West, Phys. Rev. Lett. **93**, 146601 (2004).

[8] L. P. Rokhinson, L. N. Pfeiffer, and K. W. West, Phys. Rev. Lett. **96**, 156602 (2006).

[9] G. Usaj and C. A. Balseiro, Phys. Rev. B **70**, 041301 (2004).

[10] U. Zülicke, J. Bolte, and R. Winkler, New J. Phys. **9**, 355 (2007).

[11] S. Bladwell and O. P. Sushkov, Phys. Rev. B **92**, 235416 (2015); **95**, 159901(E) (2017).

[12] A. Reynoso, G. Usaj, and C. A. Balseiro, Phys. Rev. B **75**, 085321 (2007).

[13] S. Bladwell and O. P. Sushkov, Phys. Rev. B **96**, 035413 (2017).

[14] Y. A. Bychkov and E. I. Rashba, J. Phys. C **17**, 6039 (1984).

[15] S.-T. Lo, C.-H. Chen, J.-C. Fan, L. W. Smith, G. L. Creeth, C.-W. Chang, M. Pepper, J. P. Griffiths, I. Farrer, H. E. Beere, G. A. C. Jones, D. A. Ritchie, and T.-M. Chen, Nat. Commun. **8**, 15997 (2017).

[16] R. Winkler, *Spin-orbit Coupling Effects in Two-Dimensional Electron and Hole Systems* (Springer, New York, 2003).

[17] T. Li, L. A. Yeoh, A. Srinivasan, O. Klochan, D. A. Ritchie, M. Y. Simmons, O. P. Sushkov, and A. R. Hamilton, Phys. Rev. B **93**, 205424 (2016).

[18] D. S. Miserev and O. P. Sushkov, Phys. Rev. B **95**, 085431 (2017).

[19] P. J. Simmonds, F. Sfigakisa, H. E. Beere, D. A. Ritchie, M. Pepper, D. Anderson, and G. A. C. Jones, Appl. Phys. Lett. **92**, 152108 (2008).

[20] L. W. Molenkamp, A. A. M. Staring, C. W. J. Beenakker, R. Eppenga, C. E. Timmering, J. G. Williamson, C. J. P. M. Harmans, and C. T. Foxon, Phys. Rev. B **41**, 1274 (1990).